

Proceeding Paper

# Kaoline Mapping Using ASTER Satellite Imagery: The Case Study of Kefalos Peninsula, Kos Island <sup>†</sup>

Maria Kokkaliari \* , Christos Kanellopoulos  and Ioannis Illiopoulos

Department of Geology, University of Patras, 26504 Patras, Greece; ckanellopoulos@gmail.com (C.K.); ilios@upatras.gr (I.I.)

\* Correspondence: kokkaliari\_m@upnet.gr

<sup>†</sup> Presented at International Conference on Raw Materials and Circular Economy, Athens, Greece, 5–9 September 2021.

**Abstract:** The present work aims to map kaolin occurrences on the Kefalos peninsula, SW Kos Island, Greece, through the elaboration of ASTER satellite imagery. The island of Kos is located on the eastern edge of the South Aegean Active Volcanic Arc (SAAVA) and is characterised by its complex geologic structure. During Plio-Pleistocene, the voluminous eruption of the Kos Plateau Tuff was recorded on Kefalos; the largest quaternary eruption in the Mediterranean. Kaolin is the product of hydrothermal alteration of the Pliocene volcanic rocks with rhyolitic composition. Our study emphasises the usefulness of satellite imagery combined with the Mixture Tuned Matched Filtering (MTMF) technique to detect occurrences of industrial minerals, kaolin-group minerals in this case, either in terms of raw mineral exploitation or by mapping hydrothermal alteration.

**Keywords:** ASTER; Kos island; Kefalos; industrial minerals; hydrothermal alteration; kaolinisation; MTMF algorithm



**Citation:** Kokkaliari, M.; Kanellopoulos, C.; Illiopoulos, I. Kaoline Mapping Using ASTER Satellite Imagery: The Case Study of Kefalos Peninsula, Kos Island. *Mater. Proc.* **2021**, *5*, 76. <https://doi.org/10.3390/materproc2021005076>

Academic Editor: Evangelos Tzamos

Published: 10 December 2021

**Publisher's Note:** MDPI stays neutral with regard to jurisdictional claims in published maps and institutional affiliations.



**Copyright:** © 2021 by the authors. Licensee MDPI, Basel, Switzerland. This article is an open access article distributed under the terms and conditions of the Creative Commons Attribution (CC BY) license (<https://creativecommons.org/licenses/by/4.0/>).

## 1. Introduction

The main objective of this article is to identify through remote sensing kaolin occurrences, which are products of the hydrothermal alteration of volcanic rocks, on the Kefalos peninsula, NW Kos Island, Greece. In the literature, the contribution of satellite imagery in cases of hydrothermal alteration has been extensively appraised [1–8] since important information about cost-effective mineral occurrences in the earth's surface are often deduced. The spectral properties of target minerals can help us recognise and map sites of interest with potential economic value. However, the South Aegean Active Volcanic Arc (SAAVA) has not been thoroughly studied through remote sensing, even though its complex geological structure has aroused the interest of many researchers [9–20].

Kaolin occurrences in Kefalos are related to the Pliocene volcanic rocks with rhyolitic composition. Their mineralogical composition includes quartz, Na-plagioclase, alkali-feldspar, and amorphous volcanic glass, characterised by perlitic texture. The kaolinisation process in volcanic rocks on the Kefalos peninsula has been studied [21–25] by means of geochemical analysis, mineralogical study and spectroscopical methods.

In the present study, we used accessible free multispectral satellite Advance Spaceborne Thermal Emission and Reflection Radiometer (ASTER) data and the spectral signatures of characteristic minerals from the USGS spectral library. Using laboratory spectra of kaolinite, dickite and kaolinite/smectite as pure endmembers and the Mixture-Tuned Matched Filtering Algorithm (MTMF), we were able to identify kaolin occurrences.

## 2. Geological Settings

The island of Kos (Figure 1) is located at the north-eastern edge of the SAAVA, where the African oceanic crust is subducted under the 30 km thick Aegean micro-plate [26] at

a rate of 1 cm/year [19,27,28]. Kos comprises mainly of volcanic rocks on a Paleozoic–Mesozoic carboniferous sedimentary basement that was deformed during the Tertiary by the Hellenide orogeny [29]. I-type peraluminous Miocene plutonite, with monzonitic to monzo-granitic chemical composition, intruded at Dikeos Massif [15] in folded Permo-Carboniferous sedimentary to very low-grade metamorphic rocks [20]. The intrusion caused contact metamorphic aureole to the surrounding rocks, mapped by [9]. The petrographic and geochemical characteristics of the contact metamorphic rocks were examined by [30] suggesting the contribution of hydrothermal solutions. Phase equilibrium experiments of metapelitic hornfelses estimate the depth of the intrusion to be 5–8 km approximately, and the maximum temperatures near the contact of the plutonite were about 800 °C [9,12,20]. Furthermore, the presence of amphibole- and mica-bearing lamprophyric rocks in Dikeos Massif suggest a mantle metasomatism environment [20].

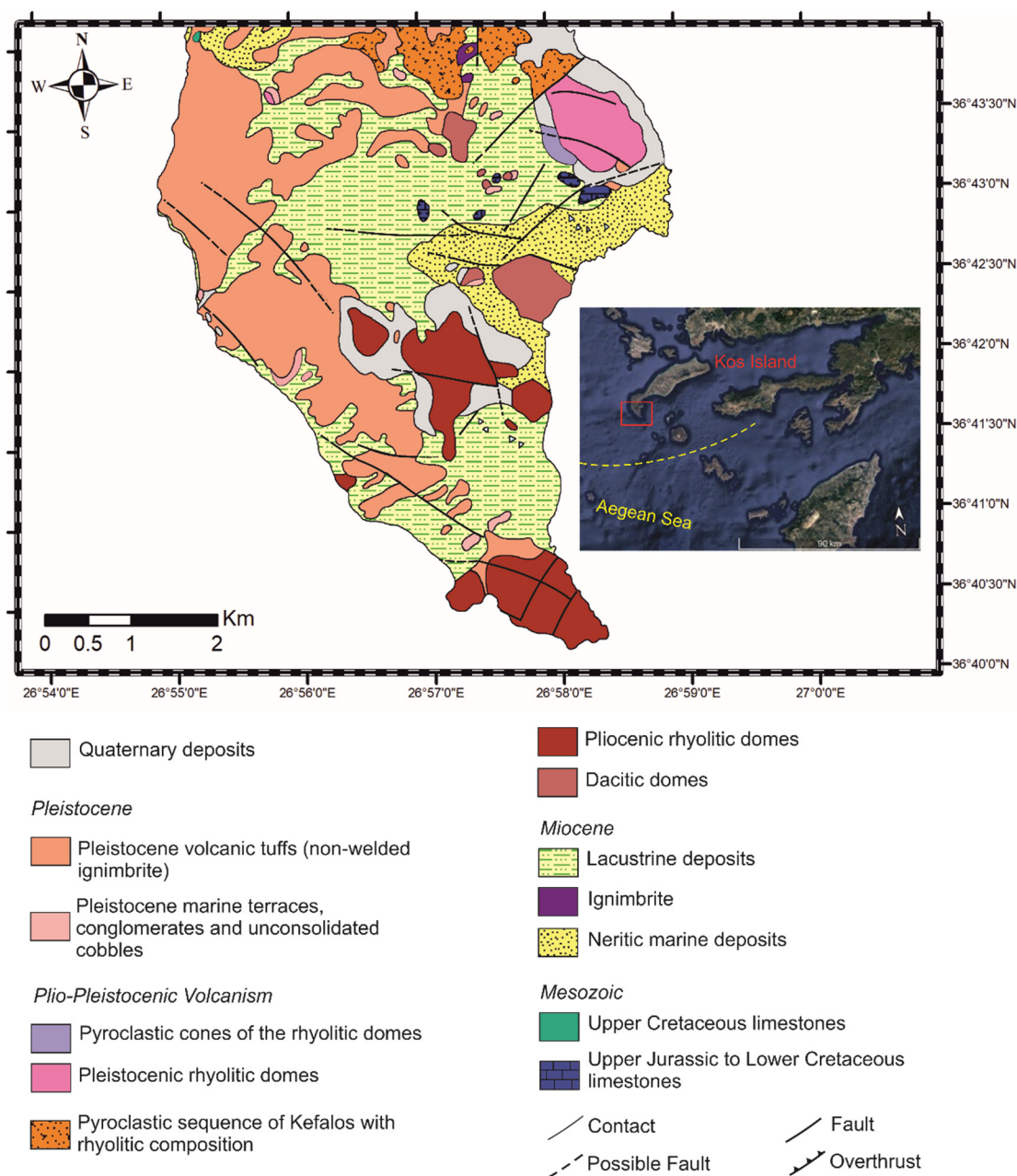


**Figure 1.** Digitised geologic map of Kefalos Peninsula (modified after [31]) and satellite view of Kos island in the south-east Aegean Sea, provided by Google Earth Pro.

Pleistocene calc-alkaline volcanic activity on the Kefalos Peninsula produced the oldest dated volcanic rock, which is now exposed as dacitic domes [17,19]. However, younger than 3 Ma rhyolitic domes and pyroclastic flows also appear in the Kefalos area [10,16,17]. The largest quaternary eruption of pyroclastic products in the eastern Mediterranean occurred at ~161 Ka, forming the voluminous Kos Plateau Tuff, evacuating more than 60 km<sup>3</sup> of ash and pumice [13]. Six major stratigraphic KPT units were mapped and studied thoroughly [32] and suggested that the pyroclastic flows travelled tens of kilometres across the sea [14].

### 3. Methodology

#### 3.1. Preprocessing Techniques

In the present study, an ASTER L1A multispectral satellite image was utilised, acquired on 9 March 2008. ASTER consists of three separate instrument subsystems that include 14 bands in the VNIR, SWIR and TIR regions (Table 1) of the electromagnetic spectrum, measuring the reflected and emitted electromagnetic radiation from the earth's surface and atmosphere [33]. Reflectance measurements in the VNIR till the SWIR wavelength region provide diagnostic information that can be used to identify rocks and their constituent minerals [33,34].

**Table 1.** Characteristics of ASTER satellite imagery [33,35].

Spectral Bands		Spectral Bandwidth ( $\mu\text{m}$ )	Spatial Resolution (m)
VNIR	1	0.52–0.60	15
	2	0.63–0.69	
	3B	0.78–0.80	
	3N	0.78–0.86	
	4	1.650–1.700	
SWIR	5	2.145–2.185	30
	6	2.185–2.225	
	7	2.235–2.285	
	8	2.295–2.395	
	9	2.360–2.430	
	10	8.125–8.475	
TIR	11	8.475–8.825	90
	12	8.925–9.275	
	13	10.25–10.95	
	14	10.95–11.65	

The pre-processing steps followed are summarised in Figure 2 and include georeferencing, radiometric calibration and atmospheric correction. The ASTER image was georeferenced in the Greek Geodetic Reference System (EGSA87). From the ASTER spectral data set, the 3N and TIR bands were excluded, and then, by applying layer stacking, the VNIR and SWIR bands were merged into one dataset so that all bands obtained the same spatial resolution (15 m). Furthermore, the ASTER image was spatially subsetted to facilitate the workflow and reduce the technical requirements of the analysis. The satellite data were radiometrically calibrated, converting DN values to radiance. Finally, the atmospheric correction was achieved using the Fast-Line-of-sight Atmospheric Analysis of the Spectral Hypercubes (FLAASH) module [36] to eliminate atmospheric effects of water vapour and aerosols and rescale raw radiance to reflectance values.

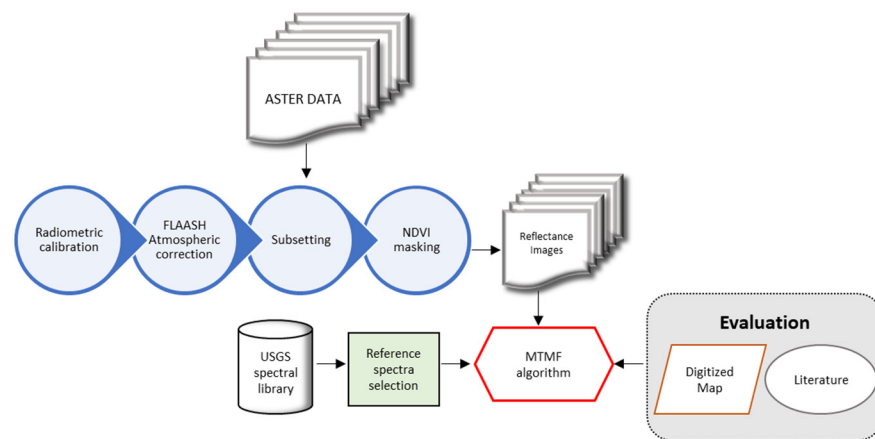


**Figure 2.** Flowchart summarising the methodology used in this study.

The Normalised Difference Vegetation Index (NDVI) was calculated to identify and exclude pixels related to vegetation, thus facilitating the classification technique. In order to extract information about NDVI, we used the following formula [7,37]:

$$(NIR - RED)/(NIR + RED) \quad (1)$$

representing wavelength values in band 2 (0.661  $\mu\text{m}$ ) and 3 (0.807  $\mu\text{m}$ ) for red and nir wavelength regions, respectively. The NDVI threshold value was set to 0.3 after carefully evaluating the study area considering Google Earth imagery.

Finally, the geologic map of western Kos from [31] was digitised in ArcGIS, to outline the geologic formations and georeferenced as well, in EGSA87.

### 3.2. Endmember Selection

Spectra from the USGS Digital Spectrum Library were collected as pure endmembers to utilise the spectral analysing algorithm. Volcanic rocks in the study area have a more acidic chemical composition, including minerals such as quartz and feldspars that are not active in the near-infrared region of the electromagnetic spectrum. Thus, the presence of minerals indicative of hydrothermal alteration exhibits diagnostic spectral absorption features. ASTER satellite imagery has been thoroughly used to discriminate hydrothermal alteration [2,4–8,38–44], considering its wide spectral coverage in the VNIR and SWIR region.

Altered rhyolitic rocks comprise mostly kaolinite, dickite, and mixed-layer kaolinite/smectite [21]. Kaolinite content increases progressively from the unaltered rhyolite to completely kaolinised rocks, whereas smectite and illite are present in small concentrations only in a few samples. The spectral features of kaolinite, dickite and kaolinite/smectite, as well as the resampled spectra to ASTER bandpasses, are displayed in Figure 3.

### 3.3. Mixture Tuned Matched Filtering (MTMF) Algorithm

Spectral unmixing techniques are used to quantify spectral information related to pure endmembers. MTMF algorithm is an advanced spectral unmixing process, differing from others in adjusting the identification of specific spectral targets without considering unwanted background or unknown pixels. In our research, we used the resampled spectra from the USGS spectral library as a reference for the spatial distribution of kaolin. This method combines the strength of the matched filter (MF) method (no requirement to be aware of all the endmembers) with physical constraints imposed by the mixing theory (the signature at any given pixel is a linear combination of the individual components contained in that pixel) [40,46]. It performs partial unmixing only by finding the abundance of a single, user-defined endmember, by maximising the response of the endmember of interest, and

by minimising the response of the unknown composite background thus “matching” the known signature [47,48].

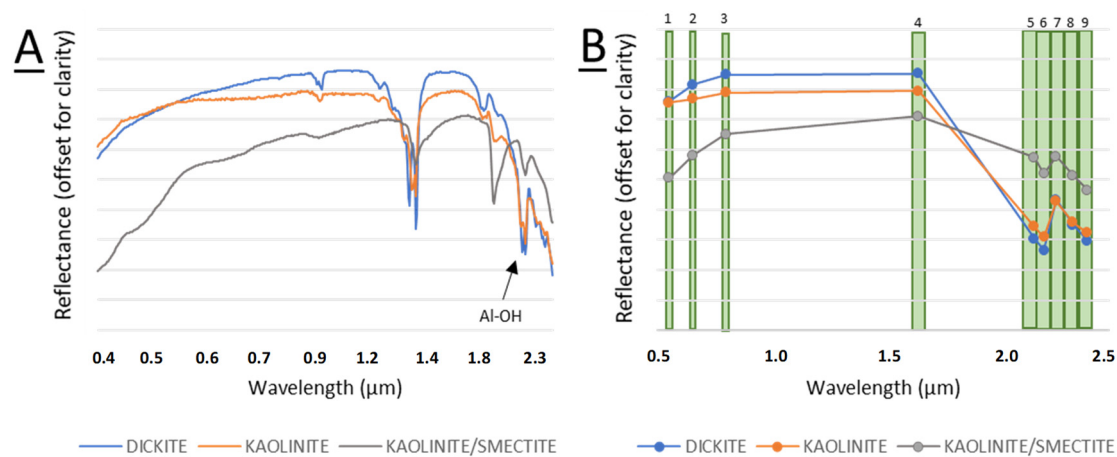


**Figure 3.** (A) USGS spectral signatures of the selected minerals used in this study [45]; (B) the resampled spectra according to the 9 VNIR and SWIR bands of the ASTER data.

The MTMF method includes an MNF transformation of the acquired reflection data [49], the matched filtering process to estimate the endmember abundance, and finally, a mixture tuning (MT) process to identify infeasible or false-positive pixels [50]. The output of MTMF is a set of rule images given as MF and infeasibility scores for each pixel related to each end member.

Since spectral targets are identified in the sedimentary background as expected (marly limestones, marls, and limestones), we used post-classification techniques to re-classify the data, excluding the unwanted identified pixels, focusing only on the volcanic rock occurrences of the studied area.

#### 4. Results and Discussion

The spectral characteristics of the selected minerals are illustrated in Figure 3. Since smectite and illite are only present in minor quantities [21], kaolinite, dickite and kaolinite/smectite spectra were used as a reference.

According to the reference spectra used, dickite has the higher reflectance values, followed by kaolinite and finally by kaolinite/smectite. Kaolinite is characterised mostly by two intense doublet absorption features at 1.39 and 1.41 μm, as well as at 2.16 and 2.20 μm, respectively. The absorption features at 1.40 μm region is associated with the inner-surface OH<sup>-</sup> groups, whereas the absorption feature at 2.20 μm is indicative of the presence of Al-OH bearing minerals [34]. Similar spectral features are exhibited in the spectrum of dickite, showing the main absorption features located at 1.38, 1.41, 2.17 and 2.20 μm. The spectrum of kaolinite/smectite differ from the other two mineral spectra because it does not exhibit doublet characteristics at 1.4 and 2.2 μm region, rather displaying one single feature centred at 1.41 and 2.20 μm. Furthermore, the kaolinite/smectite spectrum also exhibits an intense absorption feature at 1.91 μm, indicating the presence of molecular water in the mineral structure [51]. The resampled spectra of kaolinite and dickite exhibit the Al-OH diagnostic feature at the 2.2 μm region at band 6, displaying peaks at bands 4 and 7. An absorption feature at band 6 also characterises the kaolinite/smectite resampled spectrum, whereas characteristic peaks are centred at bands 4, 5 and 7.

The radiometrically calibrated and atmospherically corrected ASTER image of the Kefalos peninsula, as well as the MTMF results, are displayed in Figure 4, revealing the presence of kaolinite occurrences predominantly. The threshold value was determined based on

$$\mu + 1.5 \times \sigma \quad (2)$$

where  $\mu$  and  $\sigma$  represent the mean value and standard deviation of the relevant image.

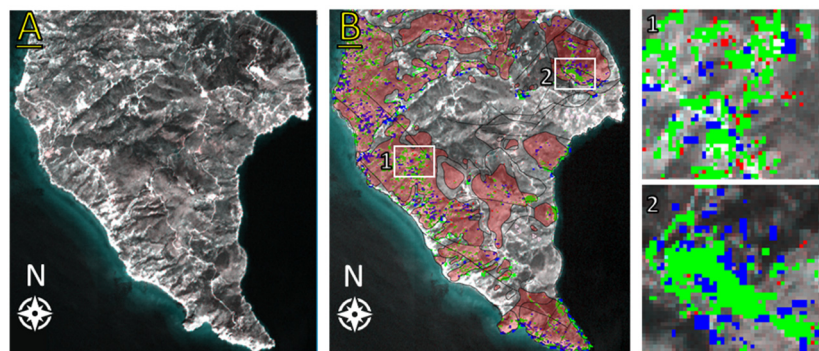


**Figure 4.** (A) Radiometrically calibrated and atmospherically corrected ASTER image of Kefalos peninsula; (B) Spatial distribution of kaolinite (green), dickite (red) and kaolinite/smectite (blue) derived from MTMF algorithm related with volcanic rocks (in red areas). Areas in numbered white boxes are displayed on the right, on a magnified scale, representing the small occurrence of dickite and kaolinite/smectite compared to kaolinite in west Kefalos (1) and the perlite quarry (2).

Several studies have used this statistic approach, usually applying  $1.5\sigma$ ,  $2\sigma$ , and  $2.5\sigma$  as thresholds to determine the alteration level of an area [8], through many different processing approaches (i.e., PCA: [8,43]; MF: [7,43]; SAM: [42]). The threshold values of kaolinite, dickite, kaolinite/smectite are 0.031, 0.039 and 0.05, respectively.

In Greece, kaolin is mainly mined periodically from Milos Island and Drama, representing different conditions of origin. It also occurs at Lesbos, Kimolos, Thera and Kos Islands, as well as Rhodope and Kilikis [52,53]. The presence of kaolinite on the Kefalos Peninsula, as an alteration product of the Pliocene volcanic rocks, agrees with the literature. Dickite is slightly exposed, mainly in the southwestern part of Kefalos (Figure 4B). Kaolinite, and to a lesser extent kaolinite/smectite and dickite, are exposed in the Pleistocene rhyolitic dome in eastern Kefalos, comprising rocks with rhyolitic compositions and perlitic, spherulitic texture. Perlite is a hydrous volcanic rock associated with volcanic fields and perlite quarries, mainly on Tertiary to Quaternary rhyolitic domes [54]. In this area, perlite occurs peripherally of the domes (Figure 4B) and is exploited due to its industrial value [52,53].

Even though there are some limitations using the library spectra as the samples are measured under certain atmospheric conditions, with specific instrumental laboratory equipment, and they may not match precisely the spectra acquired from the satellite images, we were able to utilise the MTMF algorithm to estimate their total area of distribution (Table 2).

**Table 2.** Spatial distribution of the selected mineral according to the MTMF algorithm in volcanic occurrences.

Mineral	Number of Pixels Classified	Area in Km <sup>2</sup>
Kaolinite	5879	1.323
Dickite	762	0.171
Kaolinite/Smectite	3640	0.819

## 5. Conclusions

Usage of the VNIR-SWIR spectral dataset of ASTER imagery and application of the MTMF algorithm can lead to the successful identification of kaolin occurrences in the study area. The available literature helped to verify the results and study the outcrops of the kaolinised volcanic rocks through a robust, cost-effective approach. Image processing techniques applied to ASTER satellite data can retrieve information about the hydrothermal

alteration products or even occurrences of industrial minerals, i.e., kaolinite, highlighting prospects for further investigations.

Future research includes the lithological classification of the Kefalos peninsula using image spectra and the contribution of field observations to retrieve information from multispectral images, considering as well other satellite datasets. Furthermore, the utility of laboratory analytical methods of selected samples is necessary to correlate the results from macro- to micro-scale.

**Author Contributions:** Conceptualization, M.K. and I.I.; methodology, M.K. and I.I.; software, M.K.; validation, M.K., I.I. and C.K.; formal analysis, M.K.; investigation, M.K., I.I. and C.K.; resources, M.K., I.I. and C.K.; data curation, M.K.; writing—original draft preparation, M.K.; writing—review and editing, I.I. and C.K.; visualization, M.K.; supervision, I.I.; project administration, I.I.; funding acquisition, M.K. All authors have read and agreed to the published version of the manuscript.

**Funding:** This study is a part of the Ph.D. studies of the first author and is financially supported by the “General Secretariat for Research and Technology (GSRT)” and the “Hellenic Foundation for Research and Innovation (HFRI)”, at the University of Patras.

**Conflicts of Interest:** The authors declare no conflict of interest.

## References

1. Ferrier, G.; White, K.; Griffiths, G.; Bryant, R.; Stefouli, M. The mapping of hydrothermal alteration zones on the island of Lesbos, Greece using an integrated remote sensing dataset. *Int. J. Remote Sens.* **2002**, *23*, 341–356. [[CrossRef](#)]
2. Anifadi, A.; Parcharidis, I.; Sykioti, O. Hydrothermal alteration zones detection in Limnos island, through the application of remote sensing. *Bull. Geol. Soc. Greece* **2016**, *50*, 1596–1604. [[CrossRef](#)]
3. Abdelnasser, A.; Kumral, M.; Zoheir, B.; Karaman, M.; Weihed, P. REE geochemical characteristics and satellite-based mapping of hydrothermal alteration in Atud gold deposit, Egypt. *J. Afr. Earth Sci.* **2018**, *145*, 317–330. [[CrossRef](#)]
4. Govil, H.; Gill, N.; Rajendran, S.; Santosh, M.; Kumar, S. Identification of new base metal mineralisation in Kumaon Himalaya, India, using hyperspectral remote sensing and hydrothermal alteration. *Ore Geol. Rev.* **2018**, *92*, 271–283. [[CrossRef](#)]
5. Testa, F.J.; Villanueva, C.; Cooke, D.R.; Zhang, L. Lithological and hydrothermal alteration mapping of epithermal, porphyry and tourmaline breccia districts in the Argentine Andes using ASTER imagery. *Remote Sens.* **2018**, *10*, 203. [[CrossRef](#)]
6. Khaleghi, M.; Ranjbar, H.; Abedini, A.; Calagari, A.A. Synergetic use of the Sentinel-2, Aster, and Landsat-8 data for hydrothermal alteration and iron oxide minerals mapping in a mine scale. *Acta Geodyn. Geomater.* **2020**, *17*, 311–328. [[CrossRef](#)]
7. Tompolidi, A.M.; Sykioti, O.; Koutroumbas, K.; Parcharidis, I. Spectral unmixing for mapping a hydrothermal field in a volcanic environment applied on ASTER, Landsat-8/OLI, and Sentinel-2 MSI Satellite Multispectral Data: The Nisyros (Greece) case study. *Remote Sens.* **2020**, *12*, 4180. [[CrossRef](#)]
8. Wang, Z.; Zhou, C.; Qin, H. Detection of hydrothermal alteration zones using ASTER data in Nimu porphyry copper deposit, south Tibet, China. *Adv. Space Res.* **2020**, *65*, 1818–1830. [[CrossRef](#)]
9. Altherr, R.; Keller, J.; Kott, K. Der jungtertiäre Monzonit von Kos und sein Kontakthof (Ägäis, Griechenland). *Bull. Soc. Géol. Fr.* **1976**, *18*, 403–412. [[CrossRef](#)]
10. Dabalakis, P.; Vougioukalakis, G. The Kefalos Tuff ring (W. Kos): Depositional mechanisms, vent position, and model of the evolution of the eruptive activity. *Bull. Geol. Soc. Greece* **1993**, *28*, 259–273.
11. Allen, S.R.; Cas, R.A. Rhyolitic fallout and pyroclastic density current deposits from a phreatoplinian eruption in the eastern Aegean Sea, Greece. *J. Volcanol. Geoth. Res.* **1998**, *86*, 219–251. [[CrossRef](#)]
12. Kalt, A.; Altherr, R.; Ludwig, T. Contact metamorphism in pelitic rocks on the island of Kos (Greece, Eastern Aegean Sea): A test for the Na-in-cordierite thermometer. *J. Petrol.* **1998**, *39*, 663–688. [[CrossRef](#)]
13. Allen, S.R. Reconstruction of a major caldera-forming eruption from pyroclastic deposit characteristics: Kos Plateau Tuff, eastern Aegean Sea. *J. Volcanol. Geoth. Res.* **2001**, *105*, 141–162. [[CrossRef](#)]
14. Allen, S.R.; Cas, R.A.F. Transport of pyroclastic flows across the sea during the explosive, rhyolitic eruption of the Kos Plateau Tuff, Greece. *Bull. Volcanol.* **2001**, *62*, 441–456. [[CrossRef](#)]
15. Altherr, R.; Siebel, W. I-type plutonism in a continental back-arc setting: Miocene granitoids and monzonites from the central Aegean Sea, Greece. *Contrib. Mineral. Petrol.* **2002**, *143*, 397–415. [[CrossRef](#)]
16. Pe-Piper, G.; Moulton, B. Magma evolution in the Pliocene-Pleistocene succession of Kos, South Aegean arc (Greece). *Lithos* **2008**, *106*, 110–124. [[CrossRef](#)]
17. Bachmann, O.; Schoene, B.; Schnyder, C.; Spikings, R. <sup>40</sup>Ar/<sup>39</sup>Ar and U/Pb dating of young rhyolites in the Kos-Nisyros volcanic complex, Eastern Aegean Arc (Greece): Age discordance due to excess <sup>40</sup>Ar in biotite. *Geochem. Geophys. Geosyst.* **2010**, *11*, Q0AA08. [[CrossRef](#)]
18. Piper, D.J.; Pe-Piper, G.; Lefort, D. Precursory activity of the 161 ka Kos Plateau Tuff eruption, Aegean Sea (Greece). *Bull. Volcanol.* **2010**, *72*, 657–669. [[CrossRef](#)]

19. Bachmann, O.; Deering, C.D.; Ruprecht, J.S.; Huber, C.; Skopelitis, A.; Schnyder, C. Evolution of silicic magmas in the Kos-Nisyros volcanic center, Greece: A petrological cycle associated with caldera collapse. *Contrib. Mineral. Petrol.* **2012**, *163*, 151–166. [[CrossRef](#)]
20. Soder, C.; Altherr, A.; Romer, R.L. Mantle Metasomatism at the Edge of a Retreating Subduction Zone: Late Neogene Lamprophyres from the Island of Kos, Greece. *J. Petrol.* **2016**, *57*, 1705–1728. [[CrossRef](#)]
21. Papoulis, D.; Katagas-Tsolis, P. Kaolinization processes in the rhyolitic rocks of Kefalos, Kos Island, Aegean Sea, Greece. *Bull. Geol. Soc. Greece* **2001**, XXXIV/3, 867–874. [[CrossRef](#)]
22. Papoulis, D.; Tsolis-Katagas, P.; Tsikouras, B.; Katagas, C. An FT-Raman, Raman and FTIR study of hydrothermally altered volcanic rocks from Kos Island (Southeastern Aegean, Greece). In *The South Aegean Active Volcanic Arc: Present Knowledge and Future Perspectives*; Fytikas, M., Vougioukalakis, G.E., Eds.; Elsevier: Amsterdam, The Netherlands; Boston, MA, USA, 2005; pp. 293–304. [[CrossRef](#)]
23. Papoulis, D.; Katagas-Tsolis, P.; Katagas, C. New Find of Zunyite in Advanced Argillic Alteration of. *Bull. Geol. Soc. Greece* **2004**, XXXVI, 474–480. [[CrossRef](#)]
24. Tsolis-Katagas, P.; Papoulis, D. Physical and Chemical Properties of Some Greek Kaolins of Different Environments of Origin. *Bull. Geol. Soc. Greece* **2004**, XXXVI, 130–138. [[CrossRef](#)]
25. Papoulis, D. 29Si and 27Al cpmas nmr qualitative and quantitative analysis of kaolinite and dickite in Kos island kaolins, Greece. *Bull. Geol. Soc. Greece* **2007**, *40*, 936. [[CrossRef](#)]
26. Sodoudi, F.; Kind, R.; Hatzfeld, D.; Priestley, K.; Hanka, W.; Wylegalla, K.; Stavrakakis, G.; Vafidis, A.; Harjes, H.P.; Bohnhoff, M. Lithospheric structure of the Aegean obtained from P and S receiver functions. *J. Geophys. Res.* **2006**, *111*, B12307. [[CrossRef](#)]
27. Wortel, M.J.R.; Spakman, W. Subduction and slab detachment in the Mediterranean–Carpathian region. *Science* **2000**, *290*, 1910–1917. [[CrossRef](#)]
28. Fiedrich, A.M.; Laurent, O.; Heinrich, C.A.; Bachmann, O. Melt and fluid evolution in an upper-crustal magma reservoir, preserved by inclusions in juvenile clasts from the Kos Plateau Tuff, Aegean Arc, Greece. *GCA* **2020**, *280*, 237–262. [[CrossRef](#)]
29. Pe-Piper, G.; Piper, D.J.W. *The Igneous Rocks of Greece*; Gebrüder Borntraeger: Berlin, Germany, 2002; p. 573.
30. Kokkaliari, M.; Iliopoulos, I. Petrology and geochemistry of the plutonite contact aureole, in Kos Island, Greece. In Proceedings of the 7th International Earth Science Colloquium on the Aegean Region, İzmir, Turkey, 7–11 October 2019; pp. 47–53.
31. Triantaphyllis, M. *Geological map of Greece, Western Kos (Kefalos) Sheet, 1:50000*; I.G.M.E.: Athens, Greece, 1994.
32. Allen, S.R.; Stadlbauer, E.; Keller, J. Stratigraphy of the Kos Plateau Tuff: Product of a major Quaternary explosive rhyolitic eruption in the eastern Aegean, Greece. *Int. J. Earth Sci.* **1999**, *88*, 132–156. [[CrossRef](#)]
33. Rezaei, A.; Hassani, H.; Moarefvand, P.; Golmohammadi, A. Lithological mapping in Sangan region in Northeast Iran using ASTER satellitedata and image processing methods. *Geol. Ecol. Landsc.* **2020**, *4*, 59–70. [[CrossRef](#)]
34. Hunt, G. Spectral signatures of particulate minerals in the visible and near infrared. *Geophysics* **1997**, *42*, 501–513. [[CrossRef](#)]
35. Di Tommaso, I.; Rubinstein, N. Hydrothermal alteration mapping using ASTER data in the infiernillo porphyry deposit, Argentina. *Ore Geol. Rev.* **2007**, *32*, 275–290. [[CrossRef](#)]
36. Cooley, T.; Anderson, G.P.; Felde, G.W.; Hoke, M.L.; Ratkowski, A.J.; Chetwynd, J.H.; Gardner, J.A.; Adler-Golden, S.M.; Matthew, M.W.; Bernstein, L.S.; et al. FLAASH, a MODTRAN4-based atmospheric correction algorithm, its application and validation. *IGARSS* **2002**, *3*, 1414–1418.
37. Van der Werff, H.; Van der Meer, F. Sentinel-2A MSI and Landsat 8 OLI Provide Data Continuity for Geological Remote Sensing. *Remote Sens.* **2016**, *8*, 883. [[CrossRef](#)]
38. Azizi, H.; Tarverdi, M.A.; Akbarpour, A. Extraction of hydrothermal alterations from ASTER SWIR data from east Zanzan, northern Iran. *Adv. Space Res.* **2010**, *46*, 99–109. [[CrossRef](#)]
39. Pazand, K.; Sarvestani, J.F.; Ravasan, M.R.S. Hydrothermal Alteration Mapping Using ASTER Data for Reconnaissance Porphyry Copper Mineralization in the Ahar Area, NW Iran. *J. Indian Soc. Remote Sens.* **2013**, *41*, 379–389. [[CrossRef](#)]
40. Abubakar, A.J.; Hashim, M.; Pour, A.B. Hydrothermal Alteration Mapping of Mineralogical Imprints Associated with Subtle Geothermal System Using Mixture Tuned Matched Filtering Approach on Aster Vnir and Swir Data. *ARPN J. Eng. Appl. Sci.* **2018**, *13*, 1226–1234.
41. Yousefi, S.J.; Ranjbar, H.; Alirezaei, S.; Dargahi, S. Application of Mixture Tuned Matched Filtering on ASTER Data for Hydrothermal Alteration Mapping Related to Porphyry Cu Deposits in Jabal-Barez Ranges, Kerman Copper Belt, Iran. *J. Sci. Islam* **2018**, *29*, 271–280.
42. Yousefi, S.J.; Ranjbar, H.; Alirezaei, S.; Dargahi, S.; Lentz, D.R. Comparison of hydrothermal alteration patterns associated with porphyry Cu deposits hosted by granitoids and intermediate-mafic volcanic rocks, Kerman Magmatic Arc, Iran: Application of geological, mineralogical and remote sensing data. *J. Afr. Earth Sci.* **2018**, *142*, 112–123. [[CrossRef](#)]
43. Xu, B.; Xu, Y.; Wan, B.; Wu, X.; Yi, G. Hydrothermally altered mineral mapping using synthetic application of Sentinel-2A MSI, ASTER and Hyperion data in the Duolong area, Tibetan Plateau, China. *Ore Geol. Rev.* **2018**, *101*, 384–397.
44. Fereydooni, H.; Moradzadeh, A.; Pahlavani, P.; Mojeddfifar, S. Full unmixing hydrothermal alteration minerals mapping by integration of pattern recognition network and directed matched filtering algorithm. *Earth Sci. Inform.* **2020**, *13*, 417–431. [[CrossRef](#)]
45. Clark, R.N.; Swayze, G.A.; Wise, R.; Livo, E.; Hoefen, T.; Kokaly, R.; Sutley, S.J. *USGS Digital Spectral Library splib06a*; U.S. Geological Survey, Digital Data Series 231; Geological Survey: Denver, CO, USA, 2007.

46. Zadeh, M.H.; Tangestani, M.H.; Roldan, F.V.; Yusta, I. Mineral Exploration and Alteration Zone Mapping Using Mixture Tuned Matched Filtering Approach on ASTER Data at the Central Part of Dehaj-Sarduiyeh Copper Belt, SE Iran. *IEEE J. Sel. Top. Appl. Earth Obs. Remote Sens.* **2014**, *7*, 284–289. [[CrossRef](#)]
47. Williams, A.P.; Hunt, E.R. Estimation of Leafy Spurge Cover from Hyperspectral Imagery Using Mixture Tuned Matched Filtering. *Remote Sens. Environ.* **2002**, *82*, 446–456. [[CrossRef](#)]
48. Mehr, S.G.; Ahadnejad, V.; Abbaspour, R.A.; Hamzeh, M. Using the mixture-tuned matched filtering method for lithological mapping with Landsat TM5 images. *Int. J. Remote Sens.* **2013**, *34*, 8803–8816. [[CrossRef](#)]
49. Green, A.A.; Berman, M.; Switzer, P.; Craig, M.D. A Transformation for Ordering Multispectral Data in Terms of Image Quality with Implications for Noise Removal. *IEEE Trans. Geosci. Remote Sens.* **1988**, *26*, 65–74. [[CrossRef](#)]
50. Boardman, J.W. Leveraging the High Dimensionality of AVIRIS Data for Improved Sub-pixel Target Unmixing and Rejection of False Positives: Mixture Tuned Matched Filtering. In Proceedings of the 5th JPL Geoscience Workshop, Pasadena, CA, USA, 12–16 January 1998; pp. 55–56.
51. Clark, R.N.; King, T.V.V.; Klejwa, M.; Swayze, G.A.; Vergo, N. High spectral resolution reflectance spectroscopy of minerals. *J. Geophys. Res. Solid Earth* **1990**, *95*, 12653–12680. [[CrossRef](#)]
52. Tsirambides, A.; Filippidis, A. Greece seeks mineral lifeboat. *IM* **2012**, *532*, 38–45.
53. Tsirambides, A.; Filippidis, A. Exploration key to growing Greek industry. *IM* **2012**, *533*, 44–47.
54. Bolen, W.P. *Perlite: Mineral Industry Surveys, 1990 and 1991*; US Bureau of Mines: Socorro, NM, USA, 1996.